

Supplementary Materials for:

**Prospects for Sub-Nanometer Scale Imaging of Optical
Phenomena Using Electron Microscopy**

Ze Zhang^{1,#}, Archith Rayabharam^{2,#}, Joel Martis¹, Hao-Kun Li¹, Narayana R. Aluru^{2,3}, Arun Majumdar^{1,4,5,†}

¹Department of Mechanical Engineering, Stanford University, Stanford, California 94305, United States

²Department of Mechanical Science and Engineering, University of Illinois at Urbana-Champaign, Urbana, Illinois 61801, United States

³Beckman Institute for Advanced Science and Technology, University of Illinois at Urbana-Champaign, Urbana, Illinois 61801, United States

⁴Department of Photon Science, SLAC National Accelerator Laboratory, Menlo Park, California 94025, United States

⁵Precourt Institute for Energy, Stanford University, Stanford, California 94305, United States

[#]These authors contributed equally.

[†]Corresponding author: amajumdar@stanford.edu

S1. DFT simulations

The calculation of the charge densities of the ground state and excited state are performed by a self-consistent analysis of the Density Functional Theory (DFT)¹ using the Vienna Ab initio simulation (VASP)^{2,3} package. The Perdew-Burke-Ernzerhof (PBE)⁴ exchange-correlation functional, which comes under the Generalized Gradient Approximation (GGA), was used and projected augmented wave (PAW) pseudopotentials with a 400 eV energy cutoff and Gamma-point-centered k-point of $8 \times 8 \times 1$ were used. Each unit cell consists of ~ 60 atoms, depending on the type of defect, with the simulation box having the dimensions $12.523 \times 13.014 \times 15 \text{ \AA}^3$. The convergence with respect to the grid-size and cut-off energy is shown in Fig. S1 for a sample simulation. Before the self-consistent calculations for evaluating charge densities are done, all the structures are relaxed using an energy convergence criteria of 10^{-8} eV. For calculating the charge densities in the excited state, the band energy diagram is first evaluated from the eigenvalues of the ground state, before setting the occupancies of the electrons in the excited state using the constrained GGA approach.⁵ Finally, the self-consistent calculations are repeated to calculate the charge densities. Note that the PBE potential is known to underestimate the band gap in h-BN, but the additional states in between the band gap match well with the experimental photon energies.

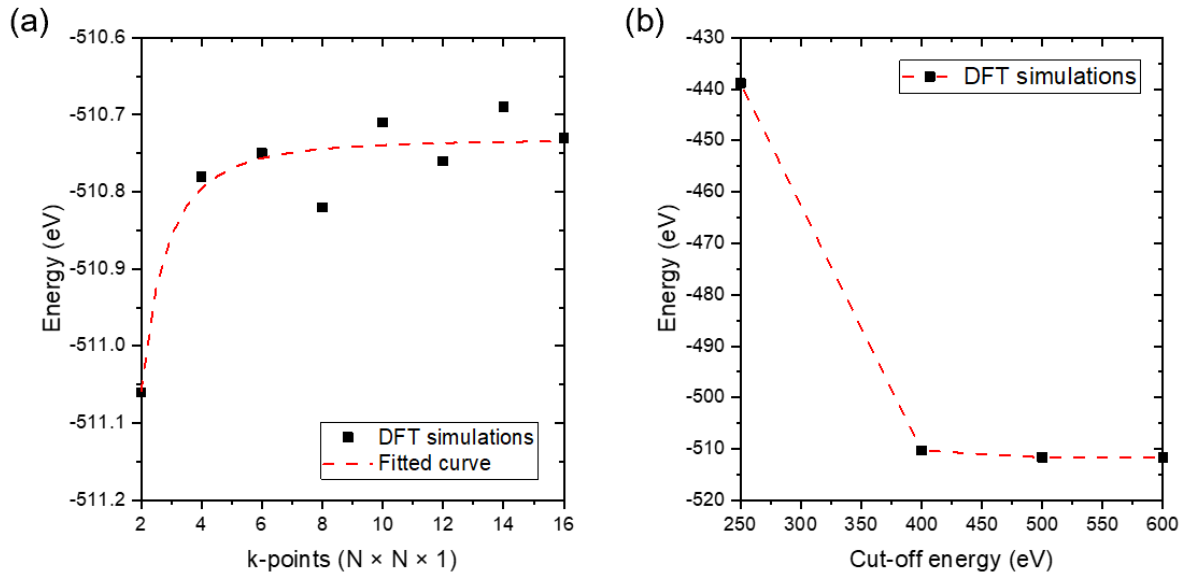


FIG. S1. Convergence of DFT simulation. (a) The energy change with the number of k-points. (b) The energy change with the cut-off energy. A k-point grid of $8 \times 8 \times 1$ and a cut-off energy of 400 eV are chosen to ensure proper convergence of the simulations and have good computational efficiency.

S2. HRTEM simulations

We first add nucleus charge as a delta function to both the ground state and excited state electron charge distribution calculated by DFT simulations. Then the 3-dimensional Poisson's equation is solved to get the ground state and the excited state electrical potentials using the spectral method. The HRTEM simulations are performed using the multislice method.^{6,7} Contrast transfer functions are then added to the exit waves. Here we considered only the defocus and the spherical aberration coefficient, leaving all high order aberration coefficients to zero. The intensity of the electron waves is captured by the camera. We add shot noise by assigning a Poisson distributed random number for each pixel.

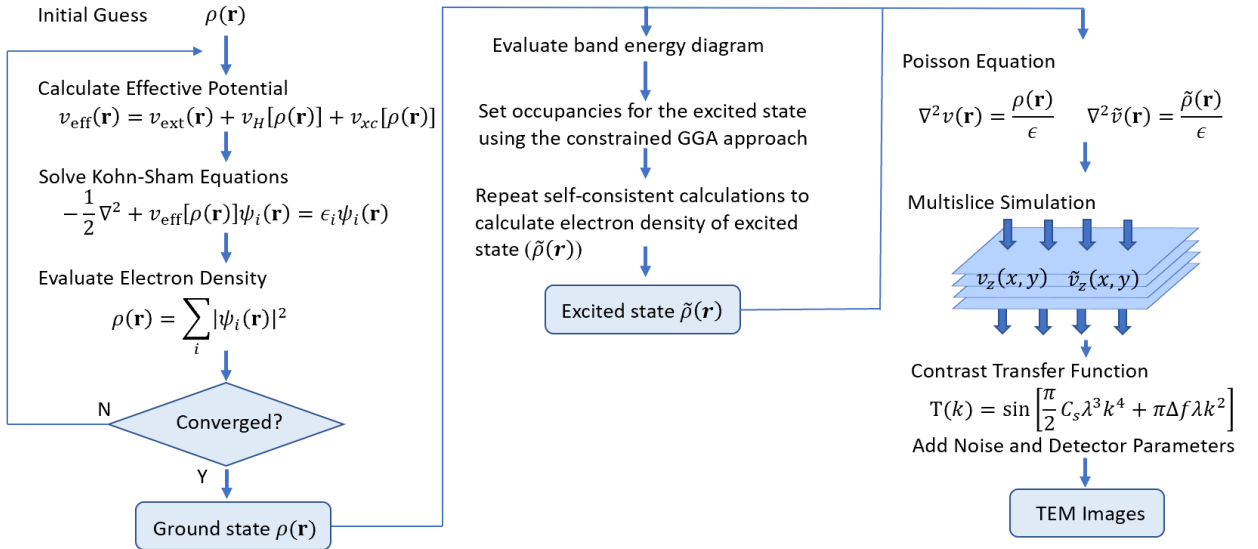


FIG. S2. Full simulation process. DFT simulation is used to calculate the ground state and the excited electron charge distribution. Multislice HRTEM simulation is then performed for both the ground state and the excited state. The ground state image provides the structural information, and the difference between the excited and the ground state images provides the optical information.

S3. Comparison between DFT and GW

Since GW simulations⁸ are more expensive computationally, we use a relatively small unit cell (~12 atoms) for the comparison. In Fig. S3, we compare the simulation results of a nitrogen missing defect in h-BN using DFT and GW methods. The Perdew-Burke-Ernzerhof (PBE)⁴ exchange-correlation functional, which comes under the Generalized Gradient Approximation (GGA), was used and projected augmented wave (PAW) pseudopotentials with a 400 eV energy cutoff and Gamma-point-centered k-point of $8 \times 8 \times 1$ were used for both the methods. The simulation box has dimensions of $10.018 \times 8.676 \times 15 \text{ \AA}^3$, with 31 atoms in its unit cell. As shown in the figures, the charge densities are quite similar for the two methods. Although GW simulation gives a slightly tighter distribution of the electron charge, this difference is partially cancelled in the difference charge distribution. In this paper, given the practical constraint of computational cost, we use DFT method to simulate the charge redistribution in larger unit cells (~60 atoms).

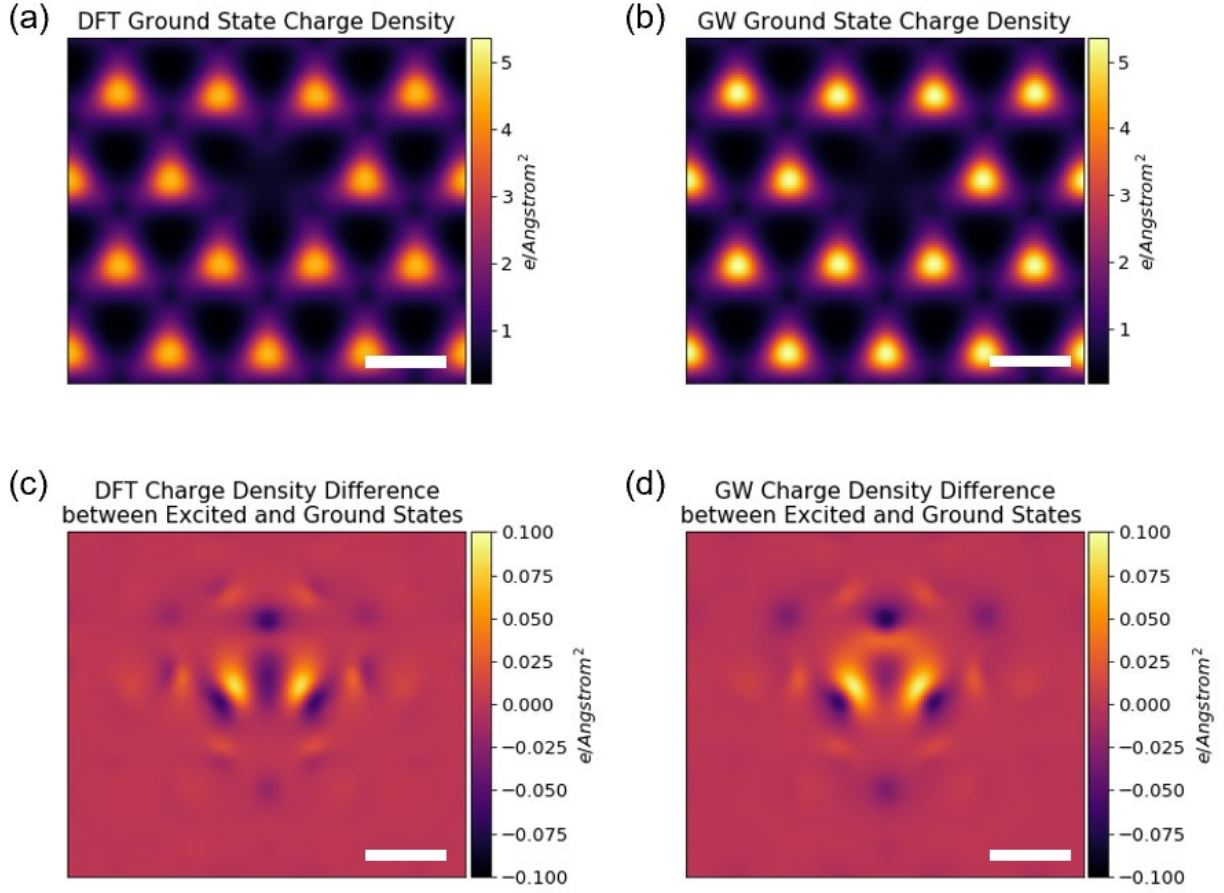


FIG. S3. Comparison of DFT and GW simulations of a missing nitrogen defect in h-BN. (a) The projected outer-shell electron charge density distribution of a missing nitrogen V_N defect simulated using the DFT method. (b) The projected outer-shell electron charge distribution using the GW method. (c) The electron charge redistribution calculated using the DFT method. (d) The electron charge redistribution calculated using the GW method. Scale bars are 2 Å.

S4. Calculation of core/shell quantum dot excited states

The first excited state of the CdS/CdTe quantum dot is calculated by solving Schrodinger's equation (Eqn. S1) for a particle in a spherically symmetric potential well using the band alignment and physical constants shown in Fig. S4.

$$-\frac{\hbar^2}{2mr^2} \frac{d}{dr} \left(r^2 \frac{d\psi}{dr} \right) + V\psi = E\psi \quad (\text{S1})$$

The two boundary conditions used at each of the two interfaces are: 1) Continuity of the wavefunction ψ ; 2) Continuity of the probability current, which reduces to continuity of $\frac{1}{m} \psi \frac{d\psi}{dr}$.

Next, we calculate the electric field using Gauss' law:

$$E(r) = \frac{-e}{4\pi\epsilon r^2} \int_0^r |\psi|^2 4\pi r'^2 dr' \quad (\text{S2})$$

Finally, the potential is calculated using $V(r) = -\int_{\infty}^r E(r') dr'$.

Since the electron/hole binding energy we get (Fig. 2) are less than 10% of the potential barrier, the exciton binding effect will only be a small correction to our current results. Therefore, we use this simple potential well model estimation to show the experimental feasibility, leaving detailed theoretical and simulation analysis for the future.

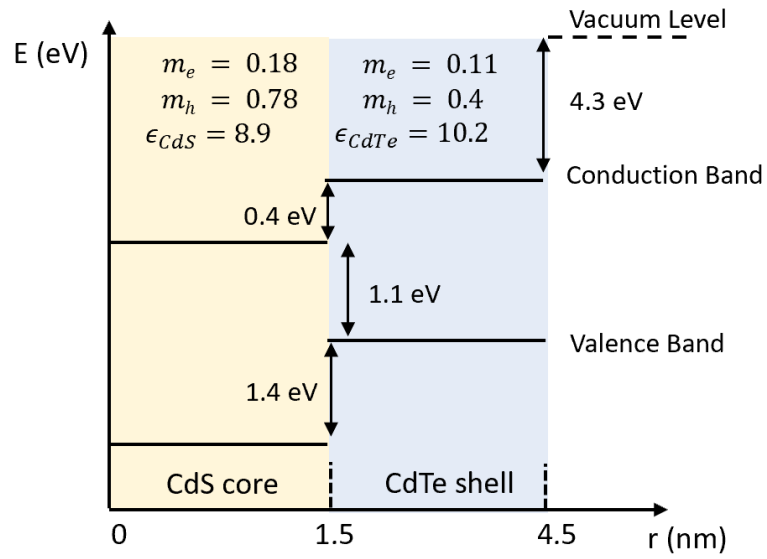


FIG. S4. Band diagram for a CdS/CdTe quantum dot. $m_e(m_h)$ represents the effective mass of an electron (hole). ϵ represents the relative permittivity of the material.

S5. Experimental characterization of TEM camera noise

We measured noise for a Gatan K3 IS direct electron camera in counting mode under dark conditions with a ~ 286 Hz frame rate. Figure S5a shows a part of a typical frame acquired. Upon acquisition of 1 second of data, the mean number of counts was calculated and was found to be ~ 1.13 electrons per pixel. This means that for every frame of acquisition, the K3 has a ‘read noise’ of $1.13/286 = 0.004$ electrons per pixel (e^-/pxl). A time series constructed by using data from multiple pixels (Fig. S5(b)), and the corresponding arrival time distribution (Fig. S5(c)) shows that the noise follows a Poisson distribution.

We further measure the noise level of the K3 IS camera when the electron beam is on. Figure S5(d) shows the results by taking three time series, which are 100 frames at 5 frames per second (fps), 200 frames at 10 fps, 319 frames at 319 fps, respectively. The mean and standard deviation for every pixel is calculated for each time series and plotted as blue dots. All results follow the same square root dependence (red curve) suggesting that shot noise is dominant.

Therefore, the signal to noise ratio (SNR) for a dose rate per pixel D , camera frame rate f and acquisition time T is $SNR = \frac{DT}{\sqrt{DT+0.004fT}}$. For the dose rate we consider ($D = 100$ $e^-/\text{per pixel/second}$ for the PAMELA image), we see that $SNR = \frac{100T}{\sqrt{100T+0.004fT}} = \frac{100\sqrt{T}}{\sqrt{100+0.004f}}$. At typical operating frequencies (~ 10 s of Hz), the noise contribution is less than 1% of shot noise. Hence, the camera noise for the K3 IS is insignificant and can be neglected even at the camera’s maximum operating frequency (1500 Hz).

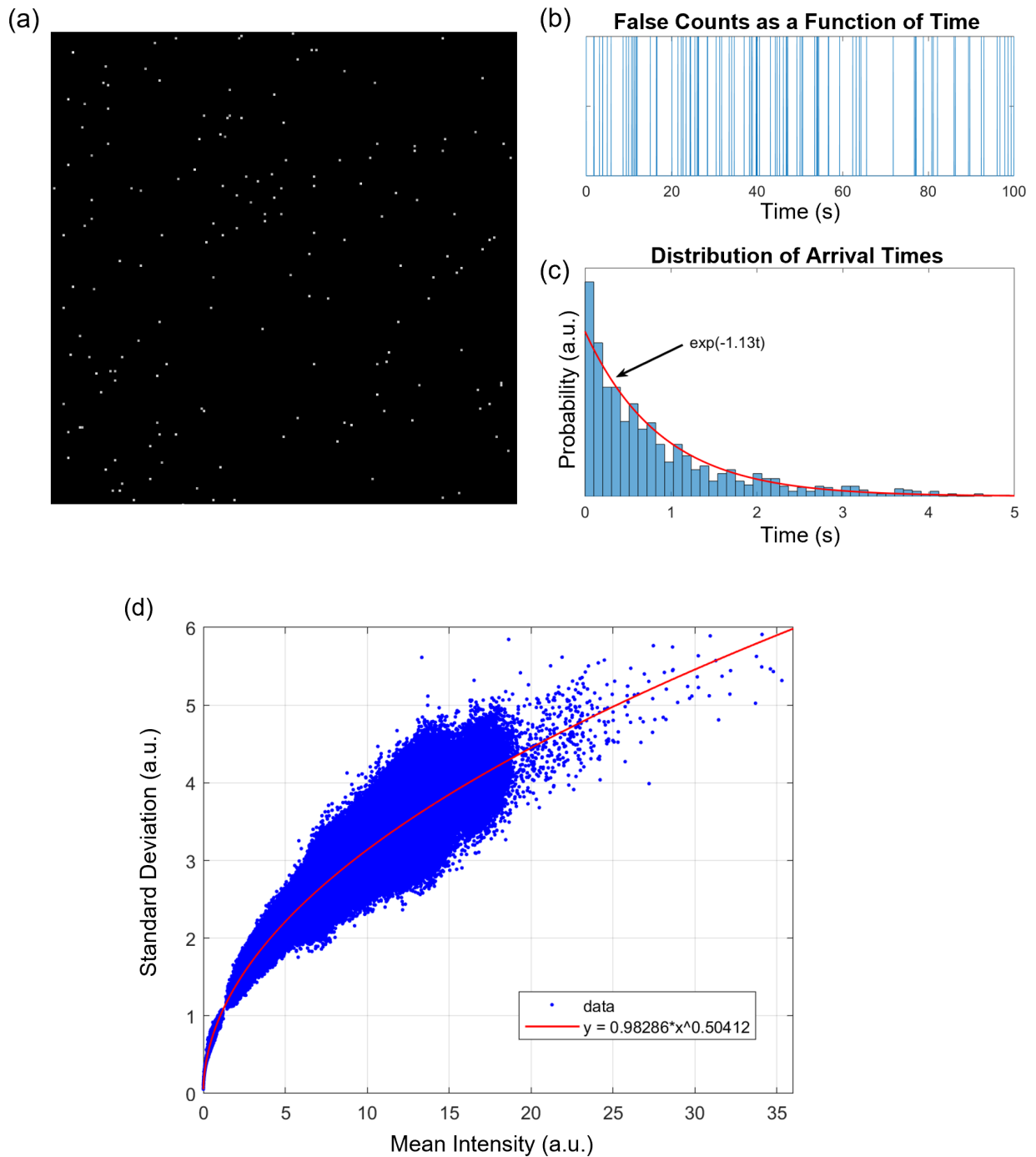


FIG. S5. (a) Part of one frame acquired with the K3 IS at ~ 300 Hz under dark conditions. (b) Typical false count time series. (c) Distribution of arrival times constructed from the time series. (d) Shot noise measurements with electron beam on. Blue dots are calculated standard deviation and mean intensity of every pixel, and the red curve is the fitting result. It is clear

that the standard deviation scales as the square root of the mean value for each pixel, which is expected for Poisson's distribution.

S6. Simulation results of other type of defects in h-BN

In the main text, we show the simulation results of an anti-site nitrogen vacancy $N_B V_N$ defect in a monolayer h-BN (Fig. 2). Here we show the results for other common types of defects like a boron missing V_B defect (Fig. S6) and a two-atom missing $V_B V_N$ defect (Fig. S7) in a monolayer h-BN. The electron phase differences between the ground states and the excited states (Fig. S6(e), S7(e)) preserve the atomic scale features from the charge density distributions (Fig. S6(f), S7(f)). By choosing different laser wavelengths, we can selectively excite certain type of defects and image the electron redistribution of the photoexcited states.

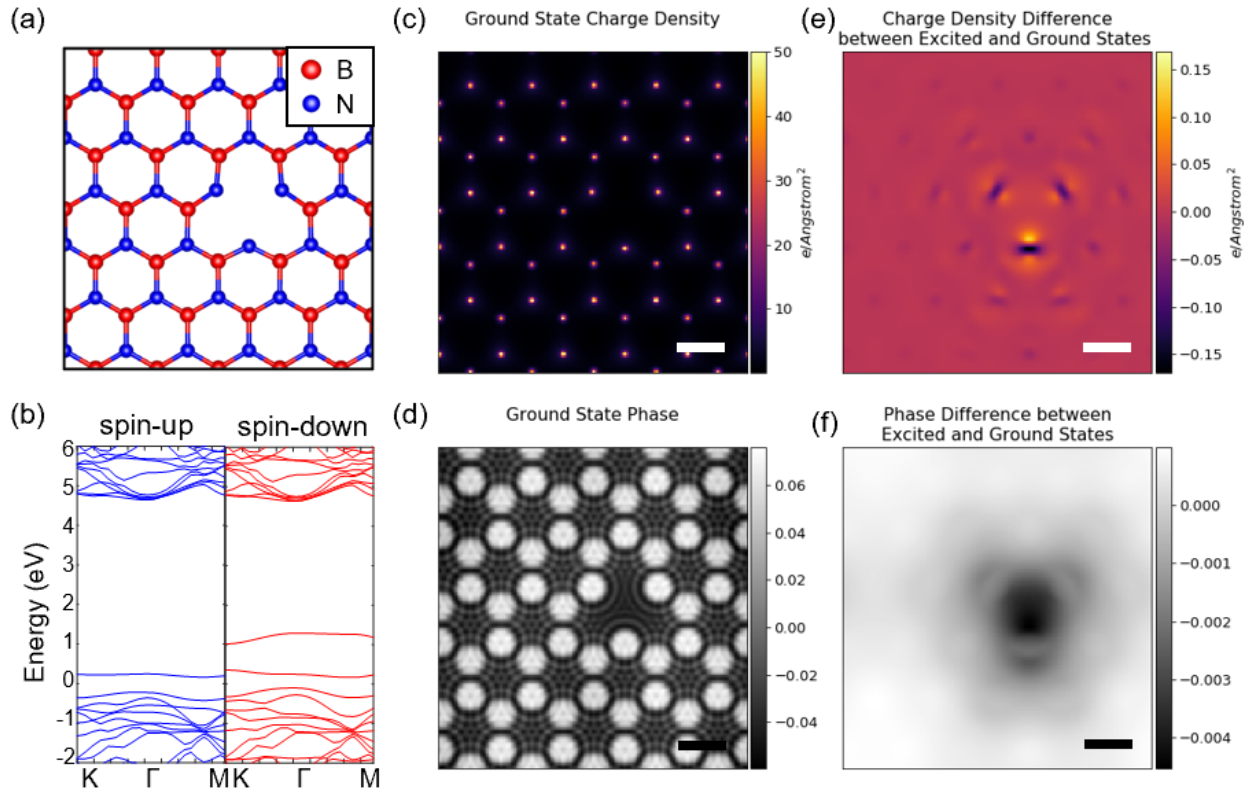


FIG. S6. Simulation results of a boron missing V_B defect in a monolayer h-BN. (a) Atomic structure and (b) Spin-polarized band structure of the defect. (c) Ground state projected charge density distribution. (d) Phase change of the exit electron beam after going through the sample at the ground state. (e) Charge redistribution due to photoexcitation. (f) The difference of phase change between the photoexcited state and the ground state. The electron phase change is simulated using 60 keV incident electron beam energy. Scale bars are 2 Å.

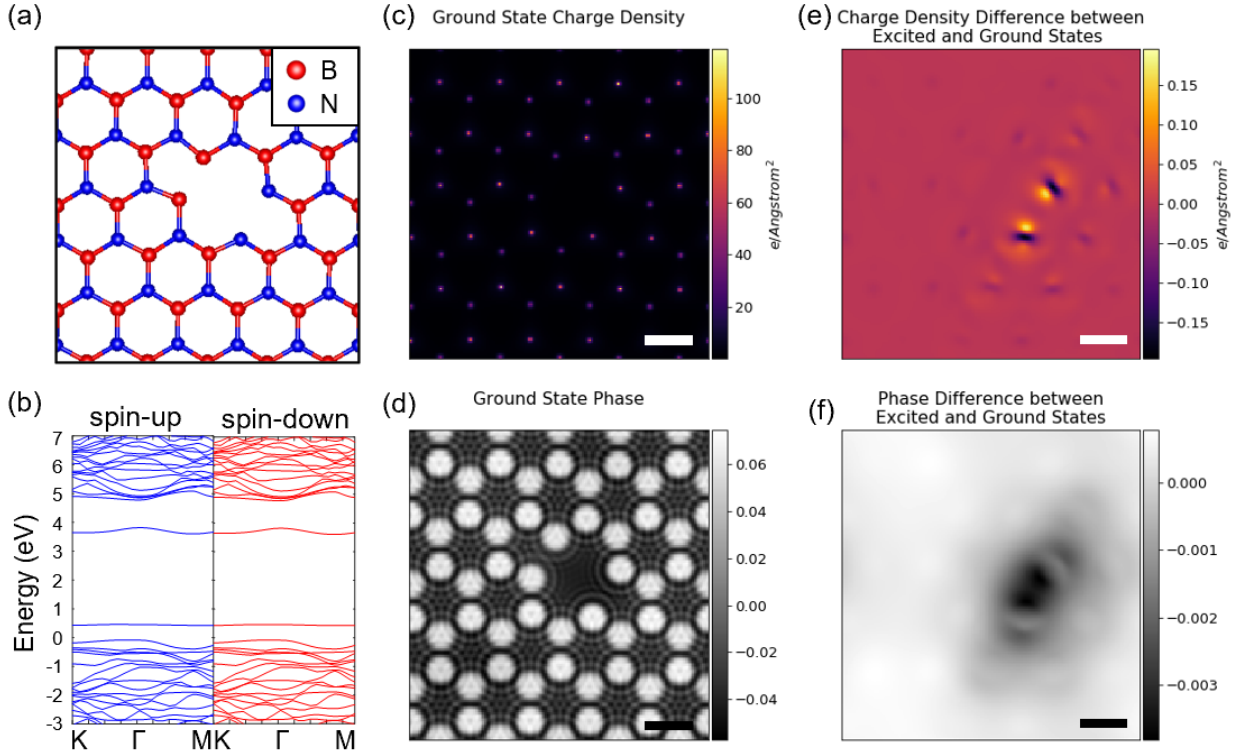


FIG. S7. Simulation results of a two-atom missing $V_B V_N$ defect in a monolayer h-BN. (a) Atomic structure and (b) Spin-polarized band structure of the defect. (c) Ground state projected charge density distribution. (d) Phase change of the exit electron beam after going through the sample at the ground state. (e) Charge redistribution due to photoexcitation. (f) The difference of phase change between the photoexcited state and the ground state. The electron phase change is simulated using 60 keV incident electron beam energy. Scale bars are 2 \AA .

S7. Dependence on TEM acceleration voltage

In high resolution TEM imaging, the image contrast varies with different acceleration voltages. Figure S8 shows the simulated maximum phase contrast change due to photoexcitations for a two-atom missing $V_B V_N$ defect in a monolayer h-BN. The phase contrast increases for lower acceleration voltage. And this trend holds for other materials systems as well. Commonly used accelerating voltages in commercial TEMs are marked with red circles. Since 30 kV TEMs are relatively rare, we choose 60 kV accelerating voltage for all the simulations in the main text.

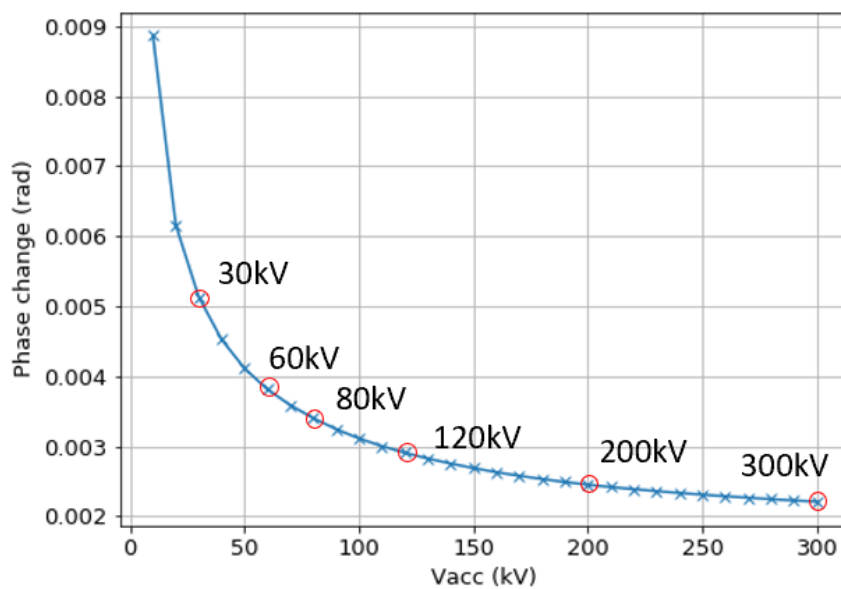


FIG. S8. Phase contrast changes as a function of accelerating voltages of a two-atom missing $V_B V_N$ defect in a monolayer h-BN. Commonly used accelerating voltages in commercial TEMs are marked with red circles.

S8. Effects of the excited states lifetime

In this paper, we mainly discuss the imaging of the excited states at the steady state. Samples can be excited using a continuous wave laser with chosen wavelengths. Although we do not explicitly discuss the time scale involved, excited states with different lifetimes will require different laser intensity to maintain a saturated occupation for the photoexcited states. Here we use a simple two-level model to discuss the basic trends of excited state occupation with the excited states lifetime and the laser intensity. More complicated models with more states and decay channels will give similar trends.

Figure S9(a) shows the energy states for a closed two-level system with excited state lifetime τ . The saturation parameter $s = \frac{\Omega_1/2}{(\omega - \omega_0)^2 + 1/4\tau^2}$, where Ω_1 is the Rabi frequency and Ω_1^2 is proportional to the laser intensity I , $\hbar\omega$ is the incident photon energy, $\hbar\omega_0 = E_1 - E_0$ is the energy difference between the ground and the excited state, \hbar is the reduced Planck constant. And the fraction⁹ of electrons on the excited state is then $\frac{N_1}{N} = \frac{s}{2(s+1)}$. As seen in Fig. S9(b), as the incident laser intensity increases, the number of excited electrons increases and saturated at 50%. For an excited state with a longer lifetime, the required laser intensity to saturate the excited state is greatly reduced. Thus long lifetime is desired for the lower laser intensity needed, which will greatly reduce the laser-induced heating and drift issues during experiments.

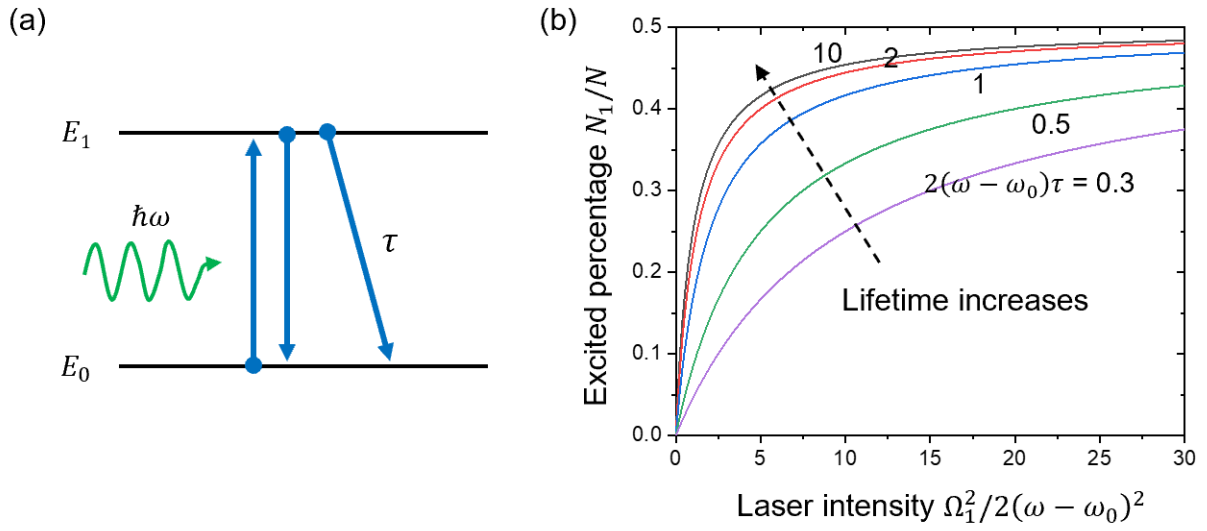


FIG. S9. Excited percentage dependence of a two-level model. (a) energy states schematics of a two-level system with excited state lifetime τ . (b) Percentage of electrons on excited state as a function of the excited state lifetime and the laser intensity.

S9. Effects of the excitation wavelengths (sub bandgap and above bandgap)

The photoexcited state electron density (Δn) can be estimated by $\Delta n = \alpha I \tau / h\nu$, where α is the absorption coefficient, I is the laser intensity, τ is the lifetime, and $h\nu$ is the photon energy. The absorption coefficient α depends on the illumination wavelength. Figure S10 shows the calculated absorption spectra of the $N_B V_N$ defect in h-BN. Those resonant absorption peaks correspond to the defect-induced in-gap states. In the main text, the excited state charge density is the first absorption peak around 1 eV. For photons below the bandgap, no photoexcitation and charge redistribution are observed. Figure S11 shows the PAMELA-TEM images for (a) below and (b) above the first resonant absorption peak. Conditions are the same as used in the main text, 120 s averaging with an electron dose rate of $10^4 \text{ e}^-/\text{\AA}^2/\text{s}$.

For core/shell CdS/CdTe quantum dots, we consider two cases – (a) the particle is illuminated by light of energy less than 1.5 eV (below the bandgap of CdTe) and (b) greater than 1.5 eV. In case (a), no electron-hole pairs are created, hence there is no charge separation and contrast in the PAMELA image. In case (b), the above bandgap illumination creates electron hole pairs which produce contrast in the PAMELA image. Figure S12 shows the PAMELA-TEM images for case (a) and case (b) after 40 s of averaging, under an electron dose rate of $10^4 \text{ e}^-/\text{\AA}^2/\text{s}$.

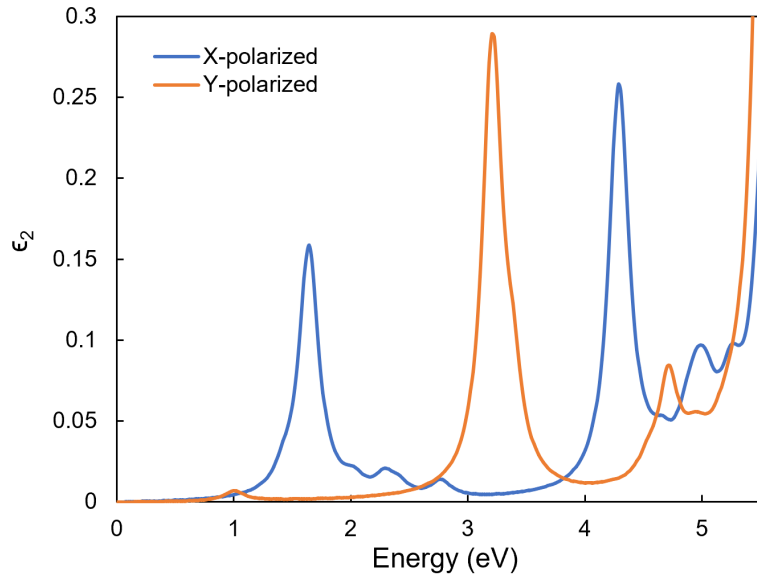


FIG. S10. Simulated imaginary dielectric tensors (absorption spectra) of an anti-site nitrogen vacancy $N_B V_N$ defect in a monolayer h-BN.

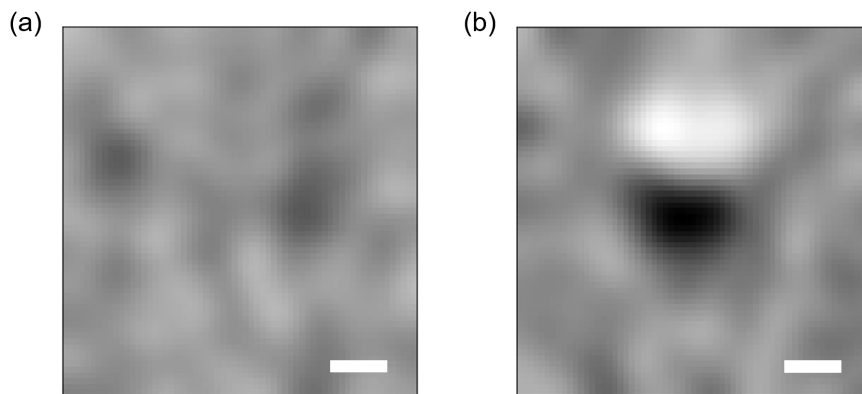


FIG. S11. AC lock-in images for an anti-site nitrogen vacancy $N_B V_N$ defect in a monolayer h-BN with (a) below and (b) above the first resonant absorption peak illumination. Images are gaussian filtered as described in the main text. Scale bars are 2 \AA .

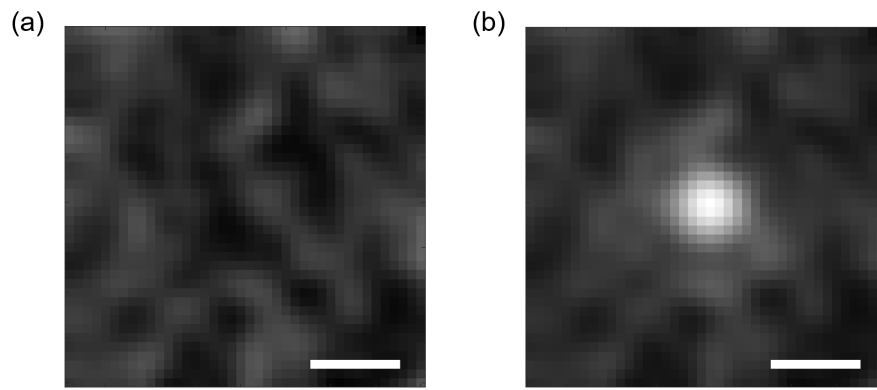


FIG. S12. AC lock-in images for a CdS/CdTe core-shell quantum dot with (a) below and (b) above the CdTe bandgap illumination. Images are gaussian filtered as described in the main text. Scale bars are 5 nm.

S10. Simulation results of an organic molecule -- Tris(bipyridine)ruthenium(II) (Ru(bpy)₃²⁺)

Tris(bipyridine)ruthenium(II) (Ru(bpy)₃²⁺) is a transition metal complex widely used in optical chemical sensing and photoelectrochemistry.¹⁰⁻¹² It can be integrated with nucleosides as luminescent moieties.¹² When photoexcited, Ru(bpy)₃²⁺ exhibits metal-to-ligand charge transfer involving an electron going from a singlet to a triplet state, which results in the excited state having an exceptionally long lifetime, of the order of hundreds of nanoseconds at room temperature.¹¹ Here, we show that PAMELA-TEM allows us to directly visualize this charge transfer process at the atomic scale for the first time.

Figure S13(a) and (b) show the charge distribution for the ground state of Ru(bpy)₃²⁺ and the charge redistribution upon photoexcitation, respectively. It is observed that photoexcitation leads to the transfer of one electron from the Ruthenium atom to the ligands. The simulated electron phase difference image (Fig. S13(d)) shows a 3 Å diameter spot corresponding to the location of the localized charge prior to photoexcitation. Adding camera pixelation (1 Å/pixel) and shot noise, we see in (Fig. S13(e)) that photoexcitation contrast becomes visible with a net electron dose of about 10⁶ e⁻/Å², requiring 100 – 500 seconds imaging time with a dose rate of 10⁴ e⁻/Å²/s.

Organic molecules such as Ru(bpy)₃²⁺ are highly susceptible to radiolysis in addition to knock-on damage, and can typically withstand only about 100 - 1000 e⁻/Å² before degradation.¹³ In cryo-EM, averaging over many low contrast images of similar biomolecules can provide atomic scale imaging of highly dose sensitive proteins. Such averaging method can be applied for PAMELA-TEM as well.

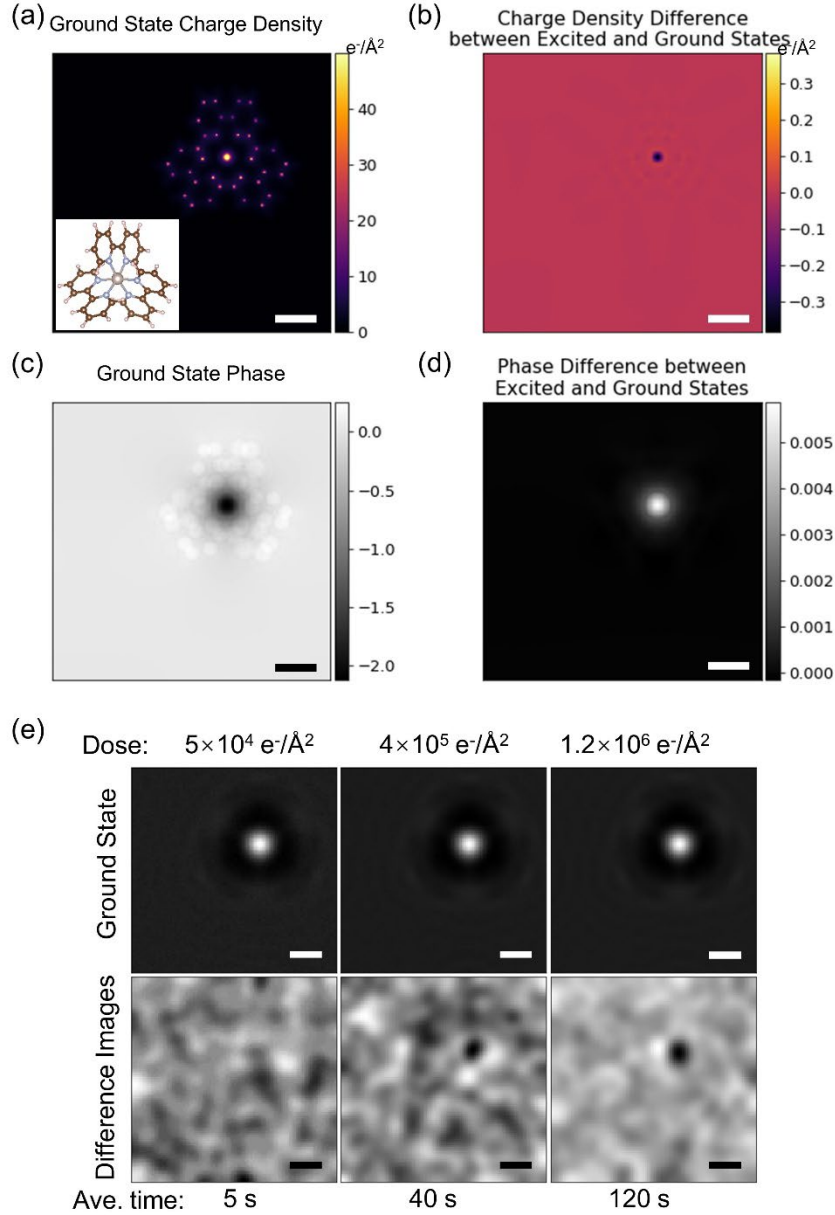


FIG. S13. Simulation results of Ru(bpy)₃²⁺. (a) Ground state projected charge density distribution. Inset is the atomic structure. The contrast is adjusted that the center Ru is saturated to make other atoms visible. (b) Charge redistribution due to photoexcitation. (c) Phase change of the exit electron beam after going through the sample at ground state. (d) The difference of phase change between the photoexcited state and the ground state. The electron phase change is simulated using 60 keV incident electron beam energy. (e) Final TEM images of the ground

state and difference between the excited and the ground state with different doses and averaging time. Defocus = -30 nm, Cs = 70 μm . Scale bars are 3 \AA .

References

- ¹W. Kohn and L. J. Sham, *Phys. Rev.* **140** (4A), A1133 (1965).
- ²G. Kresse and J. Furthmüller, *Comput. Mater. Sci.* **6** (1), 15 (1996).
- ³G. Kresse and J. Furthmüller, *Phys. Rev. B* **54** (16), 11169 (1996).
- ⁴J. P. Perdew, K. Burke, and M. Ernzerhof, *Phys. Rev. Lett.* **77** (18), 3865 (1996).
- ⁵M. Levy and Á. Nagy, *Phys. Rev. Lett.* **83** (21), 4361 (1999).
- ⁶E. J. Kirkland, *Advanced computing in electron microscopy*. (Springer, 1998).
- ⁷J. Madsen, PyQSTEM (<https://github.com/jacobjma/PyQSTEM>, 2017).
- ⁸M. Shishkin and G. Kresse, *Phys. Rev. B* **75** (23), 235102 (2007).
- ⁹G. Grynberg, A. Aspect, and C. Fabre, *Introduction to quantum optics: from the semi-classical approach to quantized light*. (Cambridge university press, 2010).
- ¹⁰K. Kalyanasundaram, *Coord. Chem. Rev.* **46**, 159 (1982).
- ¹¹G. Orellana and D. García-Fresnadillo, in *Optical Sensors* (Springer, 2004), Vol. 1, pp. 309.
- ¹²K. K.-W. Lo, in *Photofunctional Transition Metal Complexes* (Springer, 2006), pp. 205.
- ¹³R. F. Egerton, P. Li, and M. Malac, *Micron* **35** (6), 399 (2004).